Solar Energy Materials & Solar Cells 277 (2024) 113124

Contents lists available at ScienceDirect

Solar Energy Materials and Solar Cells

journal homepage: www.elsevier.com/locate/solmat

Comprehensive study of photoluminescence and device properties in $Cu_2Zn(Sn_{1-x}Ge_x)S_4$ monograins and monograin layer solar cells

İdil Mengü [a,*], Katri Muska [a], Maris Pilvet [a], Valdek Mikli [a], Evelina Dudutienė [b], Rokas Kondrotas [c], Jüri Krustok [a], Marit Kauk-Kuusik [a], Maarja Grossberg-Kuusk [a]

[a] Department of Materials and Environmental Technology, Tallinn University of Technology, Ehitajate tee 5, 19086, Tallinn, Estonia
[b] Department of Optoelectronics, Center for Physical Sciences and Technology, Saulėtekio av. 3, 10257, Vilnius, Lithuania
[c] Department of Characterisation of Materials Structure, Center for Physical Sciences and Technology, Saulėtekio av. 3, 10257, Vilnius, Lithuania

ARTICLE INFO

Keywords:
CZTS
Monograins
Germanium
Photoluminescence
Defects
Solar cells

ABSTRACT

Ge-alloying of Cu_2ZnSnS_4 is a promising strategy for producing wide-bandgap absorber materials suitable for use in tandem structures or indoor solar cell applications. Incorporating Ge can suppress Sn-related defects while maintaining the kesterite structure and *p*-type conductivity throughout the entire range of composition. In this study, $Cu_2Zn(Sn_{1-x}Ge_x)S_4$ monograins were synthesized in molten salt by the synthesis-growth method, where value x was varied from 0 to 1, with a step of 0.2. The inclusion of Ge into the crystals was confirmed by energy-dispersive X-ray spectroscopy, Raman spectroscopy, and X-ray diffraction analysis. The bandgaps of $Cu_2Zn(Sn_{1-x}Ge_x)S_4$ solid solutions were determined as $E_g = 1.50–2.25$ eV by external quantum efficiency measurement. A detailed study of temperature and laser power-dependent photoluminescence (PL) for powder crystals with x = 0, x = 0.2 and x = 0.4 revealed that the dominant recombination mechanisms originate from defect clusters involving a shallow acceptor and deep donor defect. Ge-alloying helped to suppress the harmful Sn_{Zn} donor defects, but at the same time shifted the defects' energy levels deeper into the bandgap. The obtained activation energies indicate that the acceptor defect becomes shallower with the inclusion of Ge. At the mid-temperature range (T = 60–200 K), the presence of two different recombinations was revealed in the system, originating from very closely located PL emission bands.

1. Introduction

$Cu_2ZnSn(S,Se)_4$ (CZTSSe) kesterite materials have recently received considerable interest as a promising solar cell absorber due to the attractive optical and electrical properties – high absorption coefficient ($\sim 10^{-4}$ cm^{-1}), natural *p*-type conductivity and optimum band gap for single-junction photovoltaics (PV), which is tunable depending on the S/(S + Se) ratio (1–1.5 eV) [1,2]. The constituent elements of kesterite are earth-abundant, non-toxic and it holds a record power conversion efficiency (PCE) of (14.9 %) [3] being the most advanced absorber material among the emerging inorganic thin film PV materials [4]. The primary limitation of kesterite solar cells is their open-circuit voltage (V_{OC}) deficit, which is defined by the V_{OC} voltage difference with respect to the Shockley–Queisser limit [5,6]. The main reasons behind the high V_{OC} deficit in kesterite solar cells are attributed to several factors, including low carrier concentration and lifetime, high recombination of charge carriers at the interface, high degree of cationic disorder and complex defects. Its complicated defect structure, which brings along compositional inhomogeneities, leads to band gap fluctuations and local electrostatic potential fluctuations that cause band tailing and eventually limit the V_{OC} [7,8]. Also, the cationic disorder that results from the facile exchange of Cu and Zn atoms is proposed to cause voltage-limiting band gap fluctuations. Despite the numerous efforts made to reach high ordering, a considerable concentration of Cu_{Zn} + Zn_{Cu} defect pairs is always present in the lattice leading to a spatially varying defect distribution and spatially varying bandgap. These localized regions of ordered or disordered kesterite phases will strongly contribute to bandgap fluctuations which limit V_{OC} [9].

One method for tuning the optoelectronic properties of the kesterite absorber is the cationic substitution of Sn by isoelectronic Ge. For sulfur-containing kesterite Cu_2ZnSnS_4 (CZTS), the absorber band gap can be tuned between 1.5 and 2.1 eV by controlling [Ge]/([Ge]+[Sn]) ratio from 0 to 1, also making them attractive candidates for top cells in multi-junction PV and indoor PV [10]. Moreover, Ge-alloying is expected to

* Corresponding author.
E-mail address: idil.mengu@taltech.ee (İ. Mengü).

https://doi.org/10.1016/j.solmat.2024.113124
Received 2 July 2024; Received in revised form 21 August 2024; Accepted 23 August 2024

suppress Sn-related deep defects because Ge tends to form more stable oxidation states in the kesterite structure compared to Sn. The multivalent characteristic of Sn is predicted to contribute to poor open-circuit voltage as Sn^{2+} creates deep recombination centers by trapping a pair of electrons that will reside in the localized deep gap level instead of occupying the conduction band [11–13].

Ge-alloying has demonstrated a significant positive influence on kesterite absorbers, notably improving the efficiencies of CZTSe and CZTSSe-based single-junction thin film solar cells from 6.1 to 12.3 % [14–18]. However, there are only a limited number of studies reporting on the device properties of Ge-alloyed CZTS because the bandgap deviates from the optimum bandgap for PV with Ge-inclusion [19–21]. Ge-alloying widens the bandgap over a large range while preserving the kesterite crystal structure and inherent *p*-type conductivity [22–26]. Wide bandgap kesterite material (E_g = 1.6–1.9 eV) is a promising candidate for use as a top cell absorber in a tandem approach, where the bottom cells are typically silicon-based solar cells [27,28]. However, for viable applications, top cells should meet certain criteria in terms of transparency, efficiency and stability. Yet, kesterite solar cells with absorber bandgap exceeding 1.6 eV have not been able to achieve the required PCE [29]. The main reason is typically the reduction in short circuit current (J_{SC}) due to the narrowed spectral response range, but also the change in defect properties and the mismatch in band alignment due to unoptimized buffer layer [30]. Alternatively, indoor PV is also a possible use for wide bandgap absorbers. E_g = 1.8–2.0 eV is considered to be optimal due to the spectral difference of artificial light sources such as compact fluorescent light and light-emitting diodes compared to the sunlight [31].

In kesterite-type materials, both the bandgap and defect structure are often tuned by anion or cation substitution [1,32]. One of the most efficient methods to investigate defects and recombination processes in a semiconductor is photoluminescence (PL) spectroscopy. The typical low-temperature PL spectrum of CZTS exhibits one broad asymmetrical peak situated around 1.3 eV [33–37]. The asymmetric shape of the PL band is an indication of the presence of spatial potential fluctuations due to the high defect concentration nature of kesterite. If the average depth of potential fluctuations increases, the PL band broadens [38]. The low energy side of the PL band is usually defined by the density of states function of the valence band tail while the shape of the steeper high energy side is mostly defined by the carrier distribution [39]. In kesterites, the radiative recombinations mainly originate from three different channels: band-to-band (BB) involving a free electron and a free hole, band-to-tail (BT) involving a free electron and a hole that is localized in the valence band tail and band-to-impurity (BI) involving a free electron and a hole localized at deeper acceptor defects, which do not overlap with the valence band tail. However, when potential wells localize electrons in conduction band tails, then tail-to-impurity (TI) and tail-to-tail (TT) recombinations become also possible [40].

In order to gain comprehensive insights into the recombination mechanisms, it is essential to analyze temperature and excitation-dependent PL spectra. Unfortunately, there is currently no available data regarding the low-temperature PL spectra and the corresponding dependencies for the $Cu_2Zn(Sn_{1-x}Ge_x)S_4$ series. Tseberlidis et al. [25] identified the material with x = 0.7 as the most promising candidate to produce a solar cell prototype. At T = 77 K, this material had the PL band position closest to the bandgap and the highest PL peak intensity. Its distinctive temperature-dependent behavior was characterized by a broader incline at low energies and a sharper decay at high energies. Valakh. et al. [24] also confirmed that the $Cu_2Zn(Sn_{1-x}Ge_x)S_4$ sample with x = 0.71 holds the smallest concentration of defects and its measured PL band intensity was the lowest. According to the room temperature (RT) PL spectra given by Zhu et al. [41], the PL mechanism changes throughout the series from band-dominated to tail-dominated recombination in the direction from CZTS to CZGS. It is claimed that the change occurs at x = 0.75 where the optical bandgap and PL peak position are the closest. All the data suggest that the effect of Ge inclusion on the defect structure of CZTS needs further investigation.

In this study, we synthesized $Cu_2Zn(Sn_{1-x}Ge_x)S_4$ (CZTGS) monograin powders over the entire composition range (x = 0; 0.2; 0.4; 0.6; 0.8; 1). The synthesized powder crystals were characterized using various techniques, including X-ray diffraction (XRD), scanning electron microscopy (SEM) and Raman spectroscopy. Subsequently, a detailed study was conducted on the PL dependence on temperature and excitation intensity. All CZTGS monograin powders were utilized as the absorber layer in monograin layer (MGL) solar cells. The performance of these devices was evaluated through current density – voltage ($J-V$) and external quantum efficiency (EQE) measurements.

2. Experimental

The MGL solar cell technology incorporates an absorber layer composed of monograin powders. Monograins are single-crystalline semiconductor materials with sizes varying between 36 and 140 μm for use in MGL configuration. Ge alloyed $Cu_2Zn(Sn_{1-x}Ge_x)S_4$ (CZTGS) monograin powders (x = 0; 0.2; 0.4; 0.6; 0.8; 1) were synthesized from self-synthesized (CuS) and commercially available precursors (ZnS, Sn, Ge and S) in evacuated quartz ampoules. The synthesis process was carried out at a temperature of 740 °C, utilizing potassium iodide (KI) as a flux material in its liquid phase [42,43]. High-purity precursors, each with a purity of 99.999 %, were carefully weighed in the desired molar ratios. Specifically, the molar ratio of Cu/(Zn + Sn + Ge) was set at 0.88, the ratio of Zn/Sn was maintained at 1.10, and the germanium content (Ge/(Ge + Sn)) was adjusted to the specified values of 0, 0.2, 0.4, 0.6, 0.8, and 1. To facilitate the synthesis process, flux salt was introduced into the precursor mixture at a mass ratio of precursor to flux material ($m_{precursors}/m_{flux}$) of 1:1.2. The mixture was then manually milled in an agate mortar. Subsequently, all prepared mixtures were degassed and sealed inside quartz ampoules. The furnace temperature was gradually increased from RT to 740 °C within 24 h and maintained at this elevated temperature for 168 h. After synthesis, the ampoules were removed from the furnace and allowed to cool down to RT in the ambient air. The water-soluble KI was removed by rinsing the samples with deionized water and dried in a hot-air oven at 50 °C. The resulting powders were then sieved to obtain different granulometric fractions.

The microstructure of CZTGS powder crystals was examined using a high-resolution scanning electron microscope HR-SEM Zeiss Ultra 55, which was equipped with a backscattered electron detector. For bulk composition analysis, an energy-dispersive X-ray spectroscopy (EDX) system, Bruker Esprit 1.82, equipped with an EDX-Xflash 3001 detector with an accelerating voltage of 20 kV was employed. Compositional analysis was conducted on polished crystals. The measurement error for elemental analysis is approximately 0.1 at.%.

RT Raman spectra were measured using the Micro-Raman spectrometer HORIBA LabRAM 800HR. The excitation source utilized was a Nd:YAG laser beam with a wavelength of 532 nm and it was focused on the sample with an x50 objective lens. The scattered laser light was analyzed by using an 1800 lines/mm grating monochromator and a Si CCD detector. The crystal structure was studied by XRD with a Rigaku Ultima IV diffractometer equipped with rotating 9 kW Copper anode X-ray tube (λ = 0.154 nm, at 40 kV and 40 mA) in Bragg Brentano geometry (10°–70° 2θ angle range with 0.02° step) operating with the silicon strip detector D/teX Ultra. The phase analysis and lattice parameters calculations were made by using software on Rigaku's system PDXL2.

For PL measurements, the samples were affixed to the cold finger of the closed-cycle helium cryostat (Janis SHI-4) and cooled down to 3 K. The temperature was adjusted up to RT via a temperature controller (Lake Shore Cryotronics). The PL excitation source was a diode-pumped Nd:YAG solid-state pulsed laser with a wavelength of 266 nm, pulse width of 0.6 ns and pulse repetitions rate of 19 kHz. To control the incident laser beam peak power density, gradient UV (fused silica) filters were employed, offering a range between 12 and 669 kW/cm^{-2}. The

emitted light was focused on the computer-controlled single grating monochromator (Andor SR-500i) using a 0.5 m focal length. Luminescence was dispersed by the monochromator and detected by the liquid nitrogen-cooled InGaAs detector (IGA2.2-010-LN of Electro-Optical Systems Inc).

In MGL technology, powder grains of similar size are essential. Therefore, monograins with a size fraction of 100–112 μm from each series were selected to be utilized as the absorber layer in MGL solar cells. To eliminate any potential secondary phases and precipitates that might be formed on the crystals' surfaces during the cooling process of the ampoules to RT [44], a two-step chemical etching process was employed [45]. After the chemical etching process, the treated powders were subjected to annealing at 840 °C within degassed and sealed ampoules. The post-annealing process plays a crucial role in both repairing the surface and fine-tuning the bulk composition of the crystals [44,46]. Prior to employing the powder crystals as the absorber layer in the MGL solar cell, a CdS buffer layer was deposited onto the post-annealed monograin powders using the chemical bath deposition method. After the deposition of the buffer layer, the powders were embedded within a thin epoxy layer to form a monolayer structure. The resulting membrane was then covered with transparent conductive oxide layer (*i*-ZnO and ZnO:Al) by radio frequency magnetron sputtering. To complete the process, front and back contacts were applied. A more detailed description of MGL technology can be found elsewhere [47].

The $J-V$ characteristics of MGL solar cells were measured under standard test conditions (AM 1.5, 100 mW cm^{-2}) using a Newport Oriel Class A 91195A solar simulator. The external quantum efficiency (EQE) spectra were performed on a commercial EQE measurement system (Canada, Sciencetech Inc., PTS-2-IQE). The light intensity at each wavelength was calibrated by a pyroelectric detector. The measurements were done at bias light condition and 0V bias voltage.

3. Results and discussion

3.1. Compositional and morphological analysis

Table 1 shows the EDX elemental compositions of Cu, Zn, Sn, Ge and S in the as-grown samples together with Cu/(Zn + Sn + Ge) and Ge/(Ge + Sn) composition ratios. The atomic percentages represent the mean values obtained from measuring 6 different polished individual grains for each sample, as seen in Fig. 1. Compared to the intended elemental ratios, Ge/(Ge + Sn) nicely follows the 0.2 step with very small variations. All samples except for x = 1 are in the Cu-poor and Zn-rich region, however, with the increase of Ge content, the composition approaches stoichiometry. ZnS was found to be the only secondary phase present in all samples, except x = 1 (Fig. 1 (d) and (e)), existing usually as separate crystals. ZnS, with its wide band gap (~3.6 eV) and high resistance [48], acts as a filler material in a monograin membrane and can only reduce the active area of the solar cell. All crystals have flat facets and sharp edges, which is a suitable shape for MGL technology. Ge-alloying didn't have a significant effect on the morphology. Since the samples were isothermally annealed at elevated temperatures, no elemental loss or compositional change after the annealing was expected.

3.2. Structural analysis

The crystal structure of as-grown $Cu_2Zn(Sn_{1-x}Ge_x)S_4$ monograin powders with different Ge/(Ge + Sn) ratios was analyzed by XRD, see Fig. 2(a). XRD patterns for the entire CZTGS series showed a dominant peak corresponding to the (112) orientation at 28.50 deg for CZTS and at 29.03 deg for CZGS, along with smaller peaks for the (002), (101), (110), (004), (220), (312) and (224) planes. The diffraction peaks were assigned to the tetragonal phase of Cu_2ZnSnS_4 ICDD (PDF-2 Release 2019 RDB, 01-080-4442) and Cu_2ZnGeS_4 ICDD (PDF-2 Release 2019 RDB, 01-074-8334). The diffraction peaks of CZTGS monograins shifted to higher angles with increasing Ge content, which is ascribed to the decrease in the unit cell volume due to the smaller atomic size of Ge compared to Sn [21]. The magnified view of the (112) peak is presented in Fig. 2(b), clearly showing the shift caused by Ge substitution. All peaks are accompanied by their respective doublets, exhibiting heavy overlapping at lower angles and greater separation at higher angles. The doublets are caused by the Cu-Kα2 radiation present in the diffractometer. No secondary phases could be identified because the peaks of CZTGS coincide with the characteristic XRD peaks of possible binary and ternary phases like ZnS, CuS, Cu_2SnS_3 and Cu_2GeS_3 [49]. However, the peak shift induced by the inclusion of Ge should enable the aforementioned secondary phases to become distinguishable. Still, even for the fully Ge-substituted sample, no secondary phases were observed.

The lattice parameters were calculated using the XRD patterns as $a = 5.428$ Å and $c = 10.836$ Å for CZTS and as $a = 5.339$ Å and $c = 10.490$ Å for CZGS. As seen in Fig. 3(a), the lattice parameters exhibit a linear decrease with an increase in the Ge/(Sn + Ge) ratio. This phenomenon arises from the difference in atomic size between Sn and Ge. The observed linear trend provides evidence that the CZTGS alloy series conforms to Vegard's law [50]. According to computational simulations reported by Zheng et al. [51], the tetragonal distortion parameter ($c/2a$) is used as an indicator of whether the crystals belong to the kesterite ($c/2a$) < 1 or stannite ($c/2a$) > 1 structure. This implication lies in different arrangements of Cu and Zn atoms in these structures resulting in different bond lengths of Cu-S, Zn-S or Sn(Ge)-S. In our case, ($c/2a$) exhibited values lower than unity throughout the compositional range, see Fig. 3(b), which corresponds to kesterite structure. However, the reason for the linear decrease of ($c/2a$) with increasing Ge content is not clear. A similar trend has been observed before in $Cu_2Zn(Sn_{1-x}Ge_x)Se_4$ solid solutions [52–54].

3.3. Phase analysis

Raman spectroscopy was used to analyze the phase composition of as-grown CZTGS monograins. The Raman spectra for the entire compositional range are presented in Fig. 4, showing good agreement with previously reported findings [10,13,49,55]. All spectra showed two main vibrational A modes, identified at 288 and 338 cm^{-1} for CZTS and at 297 and 361 cm^{-1} for CZGS. A blueshift was observed with increasing the Ge content for both A_1 and A_2 symmetry modes along with other characteristic peaks. Since the dominant peaks originate from the vibration modes of S atoms, it is also affected by the variations in Sn-S and Ge-S bonding [13]. The substitution of Sn by the smaller atomic size Ge leads to a change in the bond-stretching force constant between S and

Table 1
EDX elemental composition of $Cu_2Zn(Sn_{1-x}Ge_x)S_4$ monograins given with the standard deviation from the average.

Sample	Cu (at%)	Zn (at%)	Sn (at%)	Ge (at%)	S (at%)	Cu/(Zn + Sn + Ge)	Zn/(Sn + Ge)	Ge/(Ge + Sn)
x = 0	24.00 ± 0.09	13.30 ± 0.04	12.67 ± 0.06	0	50.04 ± 0.06	0.92	1.05	0.00
x = 0.2	24.13 ± 0.11	13.08 ± 0.04	10.34 ± 0.15	2.40 ± 0.14	50.06 ± 0.10	0.93	1.03	0.19
x = 0.4	24.35 ± 0.08	13.00 ± 0.11	7.79 ± 0.20	4.84 ± 0.17	50.02 ± 0.03	0.95	1.03	0.38
x = 0.6	24.65 ± 0.14	12.84 ± 0.09	5.23 ± 0.08	7.25 ± 0.27	50.03 ± 0.12	0.97	1.03	0.58
x = 0.8	24.78 ± 0.15	12.88 ± 0.09	2.78 ± 0.25	9.53 ± 0.11	50.04 ± 0.06	0.98	1.05	0.77
x = 1	25.23 ± 0.31	12.92 ± 0.14	0	12.06 ± 0.28	49.79 ± 0.43	1.01	1.07	1.00

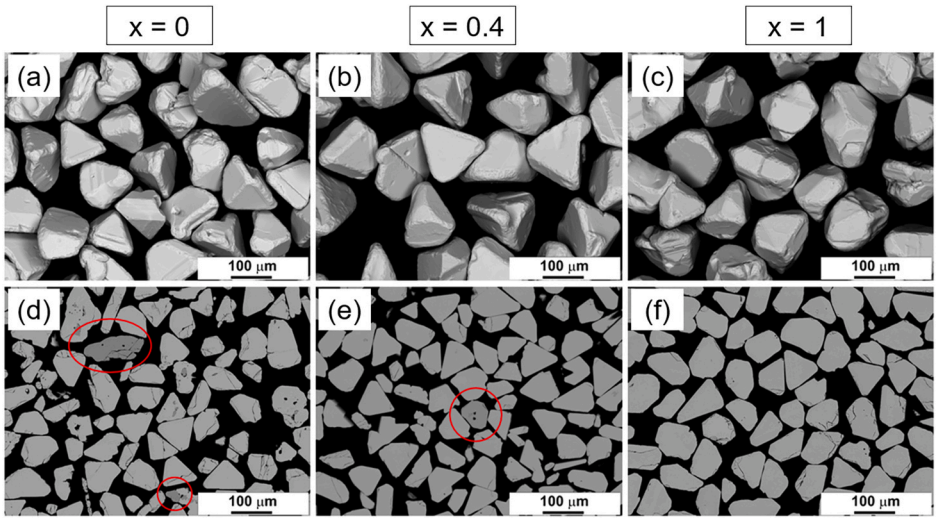

Fig. 1. SEM images of as-grown $Cu_2Zn(Sn_{1-x}Ge_x)S_4$ monograins with varying Ge content **(a, d)** x = 0, **(b, e)** x = 0.4 and **(c, f)** x = 1 **(a)–(c)** show the morphology of crystals while **(d)–(f)** indicate the cross-section images of polished samples. Dark grey areas confined with red circles in **(d)** and **(e)** correspond to the ZnS secondary phase.

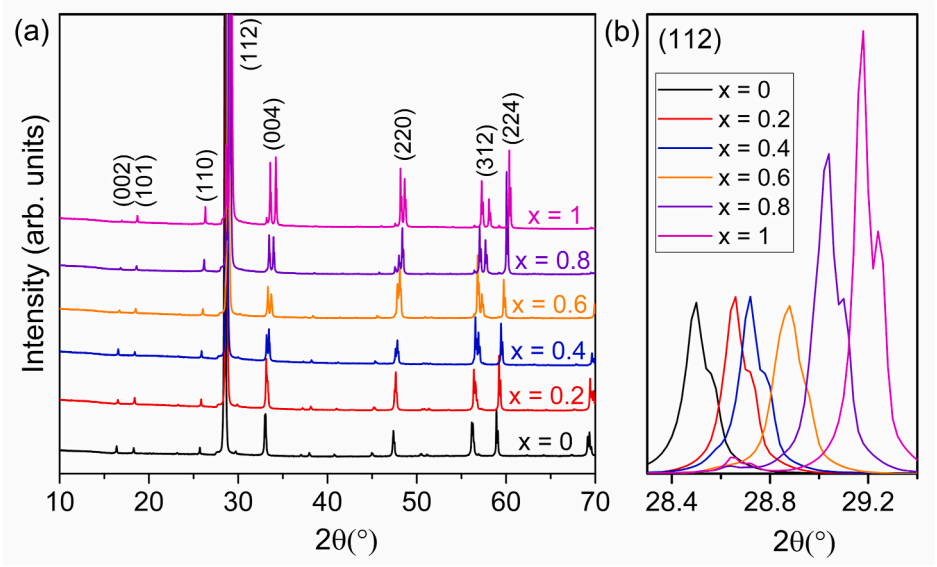

Fig. 2. XRD patterns of as-grown **(a)** $Cu_2Zn(Sn_{1-x}Ge_x)S_4$ monograins and **(b)** a magnified view of the (112) peak.

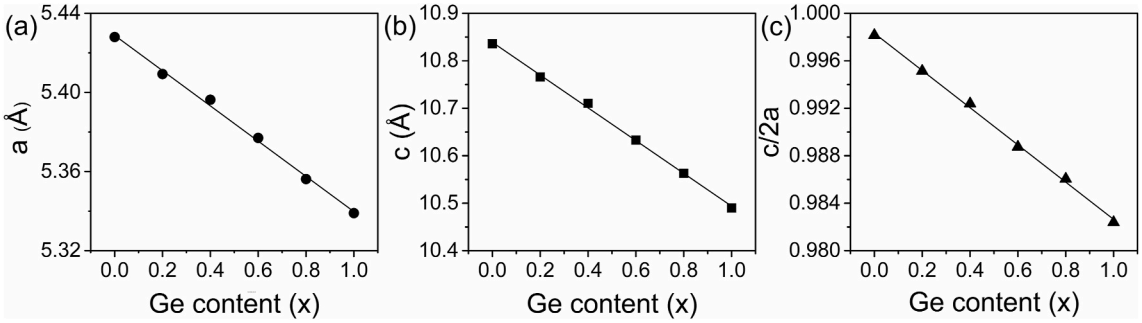

Fig. 3. **(a)**, **(b)** Lattice constants and **(c)** the tetragonal distortion parameter of $Cu_2Zn(Sn_{1-x}Ge_x)S_4$ monograins.

Sn, as well as the effective mass of S anion [56]. Accordingly, the frequency of the A_1 mode is expected to increase from x = 0 toward x = 1. For the samples with x = 0.2, 0.4, 0.6 and 0.8, the A_1 modes split into two peaks due to the coexistence of Ge-S and Sn-S bonds [53]. In two samples with the highest Ge content, the peak around 400 cm^{-1} indicated the signal enhancement attributed to the resonant effect [10]. No

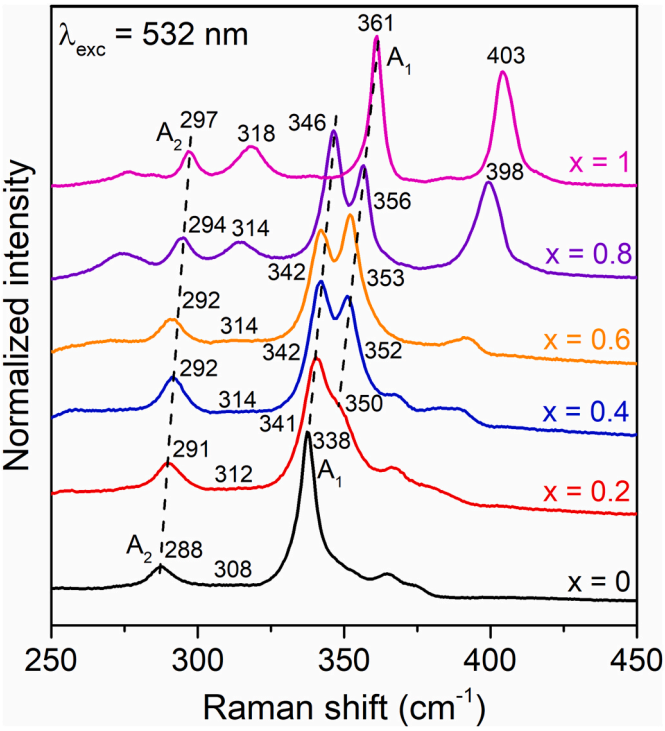

Fig. 4. Raman spectra of as-grown $Cu_2Zn(Sn_{1-x}Ge_x)S_4$ monograins.

secondary phases were observed in the examined crystals.

3.4. Device characteristics

Following the analysis of the powders, they were utilized as the absorber layer in a MGL solar cell. Table 2 shows the MGL solar cell parameters of the $Cu_2Zn(Sn_{1-x}Ge_x)S_4$ series together with the RT bandgap values determined from the EQE spectra, as shown in Fig. 5. EQE is a valuable tool to determine optical and electrical losses responsible for reducing the photocurrent collection [57]. Extrapolating the linear part in the plot $(E^*EQE)^2$ versus E gives an estimation of the bandgap. With Ge-alloying, the bandgap was tuned between 1.50 and 2.25 eV, which correlates with previously obtained values [25,53]. As the bandgap increased, a slight increase in V_{OC} values from 679 to 776 mV was observed. On the other hand, J_{SC} and η_{active} decreases with increasing Ge amount due to a narrower spectral response range for the incoming photons, particularly in the visible spectrum. The efficiency notably drops from 6.27 % at x = 0–0.87 % at x = 1. The decline in η_{active} is mainly driven by the reduction in J_{SC} which decreases substantially from 17.8 mA/cm^2 to 2.9 mA/cm^2. However, the *FF* doesn't show a regular trend and fluctuates with an overall decline, reaching a minimum of 34.1 % at x = 0.8 before slightly increasing again until x = 1. The *FF* variations can be attributed to changes in recombination losses or series resistance due to the change in composition. This trade-off between V_{OC} and J_{SC} highlights the challenge of optimizing the materials' composition and the band alignment between the buffer layer for efficient charge carrier management. Since the increase in bandgap primarily occurs from the conduction band side upon Ge-alloying, there was no improvement in terms of band alignment with CdS and an alternative buffer layer is needed. Instead of the preferred small-spike-like band alignment, cliff-like conduction band offset is expected throughout the series where the gap increases with the widening of the bandgap [30]. The overall change in device characteristics depends on many aspects and further studies are required to explain them in detail.

Table 2
The device performance parameters of $Cu_2Zn(Sn_{1-x}Ge_x)S_4$ MGL solar cells and the bandgap value (E_g) of absorber material were estimated from the EQE spectra. Since the polymer between monograins acts as a nonactive area, efficiency (η_{active}) and short circuit current density ($J_{SC\ active}$) were calculated considering a 75 % packing density of the crystals in the membrane [47].

Sample	η_{active} (%)	*FF* (%)	V_{OC} (mV)	$J_{SC\ active}$ (mA/cm^{-2})	RT E_g (eV)
x = 0	6.27	51.8	679	17.8	1.50
x = 0.2	5.68	50.6	738	15.2	1.61
x = 0.4	4.24	53.8	765	10.3	1.72
x = 0.6	2.85	42.9	772	8.6	1.88
x = 0.8	1.33	34.1	772	5.1	2.06
x = 1	0.87	38.4	776	2.9	2.25

3.5. Results of PL measurements

The PL spectra of samples measured at T = 3 K are presented in Fig. 6. Due to the high noise content and low intensity of the spectrum, x = 0.8 was excluded from the figure. As presented in Fig. 4, the Raman spectrum of x = 0.8 shows an irregular behavior in the peak splitting of the A_1 mode. Compared with x = 0.6, the relative intensity of the peak representing Ge-S bonds decreases while the peak representing Sn-S bonds increases. This might be an indication of some secondary phase formation or change in defect structure that also leads to a weak PL signal. PL measurements were done with post-treated samples where the effects of potential secondary phases were not expected. Even though the chemical etching would not remove the ZnS secondary phase, the effect of ZnS on PL data is negligible since there are few numbers of these separate ZnS monograins and since ZnS has a much higher bandgap compared with CZTS which exceeds our PL detection limit. Such a low PL intensity could be caused by the prevail of non-radiative transitions over radiative ones for the dominant recombination channel [58]. Detailed PL analysis proceeded with x = 0, x = 0.2 and x = 0.4, since the intensity of the spectra for x = 0.6 and x = 1 decreased significantly with increasing temperature. PL spectrum for x = 0.6 exhibits two peaks located at 1.05 eV and 1.52 eV, while x = 1 shows one very broad peak located at 1.33 eV. The samples with x ≥ 0.6 exhibit a distinct PL behavior characterized by broadened peaks and the appearance of additional peaks. Similarly, the sample with x = 0 is expected to contain more than one peak, as the observed peak is unusually broad for a kesterite-type material. Given that the compositional and structural analyses did not reveal any signs of non-kesterite phases or secondary phases, we can infer that this different behavior arises from a change in the recombination mechanism. Factors such as alterations in defect levels, lattice distortion and the segregation of ordered and disordered phases may contribute to this behavior and further studies must be done for the clarification. For the samples under analysis (x = 0, x = 0.2 and x = 0.4), the spectra consist of one asymmetrical band located at 1.23 eV, 1.32 eV and 1.39 eV, respectively. When the Ge content is increased, the PL peak position shifts to the higher energy side, thus following the increase in bandgap. However, the energetic difference of the PL peak position to the RT bandgap increases slightly in each step, reaching 0.27 eV, 0.29 eV and 0.33 eV for x = 0, x = 0.2 and x = 0.4. As seen in Fig. 6, the PL intensity decreases with each step of increased Ge content until x = 0.6. The sharp peak at around 1.16 eV for all spectra belongs to the laser (266 nm) harmonics, which becomes more dominant when the overall PL emission intensity decreases.

Fig. 7 shows the temperature and excitation power-dependent PL spectra of x = 0.2 and x = 0.4. Both dependencies show similar spectral shapes with changes in temperature and excitation power. PL intensity quenches gradually with increasing temperature between 3 K and 140 K and at T > 140 K the quenching continues with a much smaller rate until RT. At excitation power dependence, the same quenching trend is observed throughout the spectra.

The laser power dependence of the integrated PL band intensity Φ is shown in Fig. 8. The dependence follows the power law $\Phi \sim P^k$, where P is the excitation power and k is the exponent [59]. The k-value is

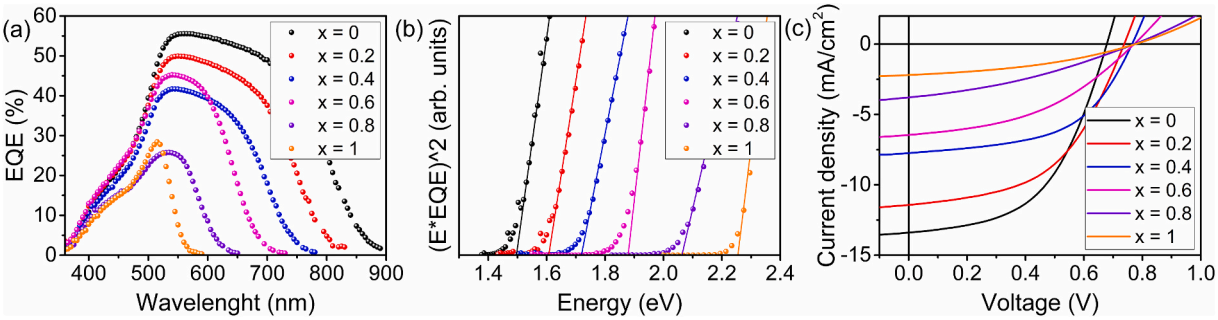

Fig. 5. (a) EQE curves for $Cu_2Zn(Sn_{1-x}Ge_x)S_4$ solar cells, **(b)** estimation of bandgap energy by plotting $(E^*EQE)^2$ versus E and **(c)** J–V curves of solar cells.

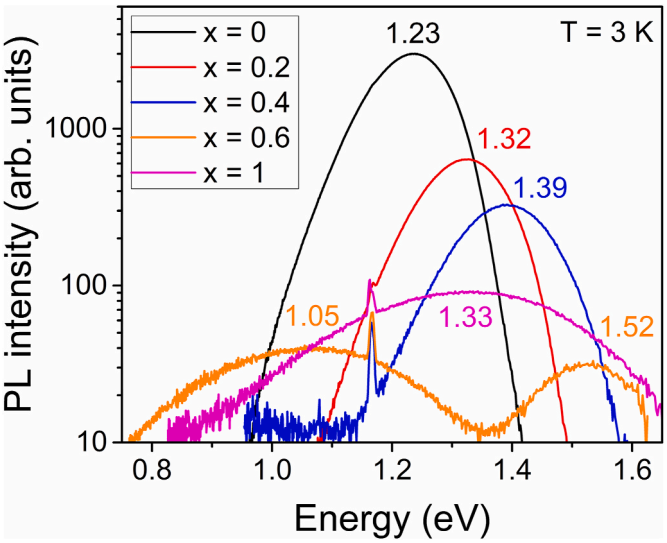

Fig. 6. Low temperature (T = 3K) PL spectra of $Cu_2Zn(Sn_{1-x}Ge_x)S_4$. The sharp peaks appearing at around 1.16 eV are belonging to the laser (266 nm) harmonics.

calculated from the gradient of linear fit as 0.45 and 0.54 for x = 0.2 and x = 0.4, respectively. All values below unity indicate that the dominant recombination in all samples is related to defect levels within the band gap. In addition, the PL bands in all samples exhibited a significant blueshift with increasing laser power. The rate of the shift increases from 10 meV to 13 meV per decade when the Ge content is increased. Although the sample x = 0 is missing from Fig. 8, it is known that excitation power dependence of CZTS monograins exhibited previously 10–15 meV blueshift/decade [60,61].

Temperature quenching of the integral intensities of the PL bands was fitted according to the exponential law [62]:

$$\Phi(T) = \Phi_0 \,/\, \left[1 + A_1 T^{3/2} + A_2 T^{3/2}\, exp(-E_A \,/\, kT)\right] \quad (1)$$

where Φ is the integrated intensity of the PL band, A_1 and A_2 are the process rate parameters and E_A is the thermal activation energy. As seen in Fig. 9, Arrhenius plots of resulting intensities for all samples follow the theoretical dependence for discrete energy levels, including the linear parts, which indicates the thermalization of acceptor defects. The calculated activation energies are 71 ± 4, 31 ± 1 and 19 ± 1 meV for x = 0, x = 0.2 and x = 0.4, respectively.

Fig. 10 presents the temperature dependence of the PL peak position (E_{max}) and full width at half maximum (FWHM) analyzed for each sample. The behavior of E_{max} is similar for all samples. At very low temperatures (3 K–40 K), it exhibits a small redshift, followed by a significant blueshift (40 K–200 K) up to a critical temperature around 200 K. Beyond this critical temperature, it shows a redshift again until RT. With Ge-substitution, the maximum shift of E_{max} increases from 49 meV to 59 meV and then to 77 meV. Again, from x = 0 to x = 0.4, the critical temperatures where E_{max} reaches its minima and maxima move slightly to lower values. Another difference observed is that the initial redshift at the very low-temperature range slowly disappears. The FWHM, on the other hand, shows a rather unusual behavior with temperature, particularly after 100 K. Initially, it increases until ~100 K, coinciding with the onset of the E_{max} blue-shift and then starts to decrease, continuing this decrease until the RT.

3.6. Shape of the PL band

At the temperature of T = 3 K, the characteristic shape of the PL bands exhibits a wide, tail-like increase on the low energy side and a steep decay on the higher energy side. Both sides can be well approximated by a Gaussian function, separately. Choosing the most appropriate fitting function is of great importance because PL I_{max} (maximum PL intensity), E_{max} and FWHM are calculated using the fitting parameters of the chosen function. This characteristic dataset is essential for the PL analysis. In this work, all measured PL spectra were fitted by the Pekarian function which gave the best empirical fitting for all samples at all temperatures [63]:

$$I(E) = I_0 \sum_{m=0}^{10} \frac{S^m}{m!} exp\left(-4\, ln\, 2 \left(\frac{E - E_0 + m\hbar\omega}{\delta} \right)^2 \right) \quad (2)$$

where $I(E)$ is PL intensity at a photon energy, I_0 is a frequency-independent constant, S is the Huang-Rhys factor, E is photon energy, $\hbar\omega$ is the phonon energy, E_0 is the position of zero phonon line and δ a Gaussian broadening of transitions. The theory of multiphonon optical absorption was first formulated by Pekar [64] and by Huang and Rhys [65]. The model was used many times to describe the shape of the emission bands of semiconductors [63,66]. The fitting for the samples x = 0, x = 0.2 and x = 0.4 at T = 3 K, 80 K and 160 K are shown in Fig. 11 proving that the selected fitting function perfectly approximates the original PL data in different temperatures. The obtained fitting parameters of the Pekarian function were then reformulated into PL parameters, presented in Table 3.

In chalcopyrites and kesterites, the high defect density results in such a small distance between defects that the electrons tend to recombine not in a discrete energy level, but rather in varied energy levels. In the case of a p-type semiconductor, the most typical radiative transition involves localized holes within potential wells in the valence band tail [67]. These tail states are known to be one of the root causes limiting the transport of photo-generated carriers and formed due to the high concentration of defects, non-stoichiometry and compositional inhomogeneities. These factors eventually lead to potential and bandgap fluctuations [39,68,69].

In the PL spectra, the average amplitude of fluctuations can be estimated from the low-energy side of the PL band, since this part reflects the density of states affected by the depth of fluctuations [40].

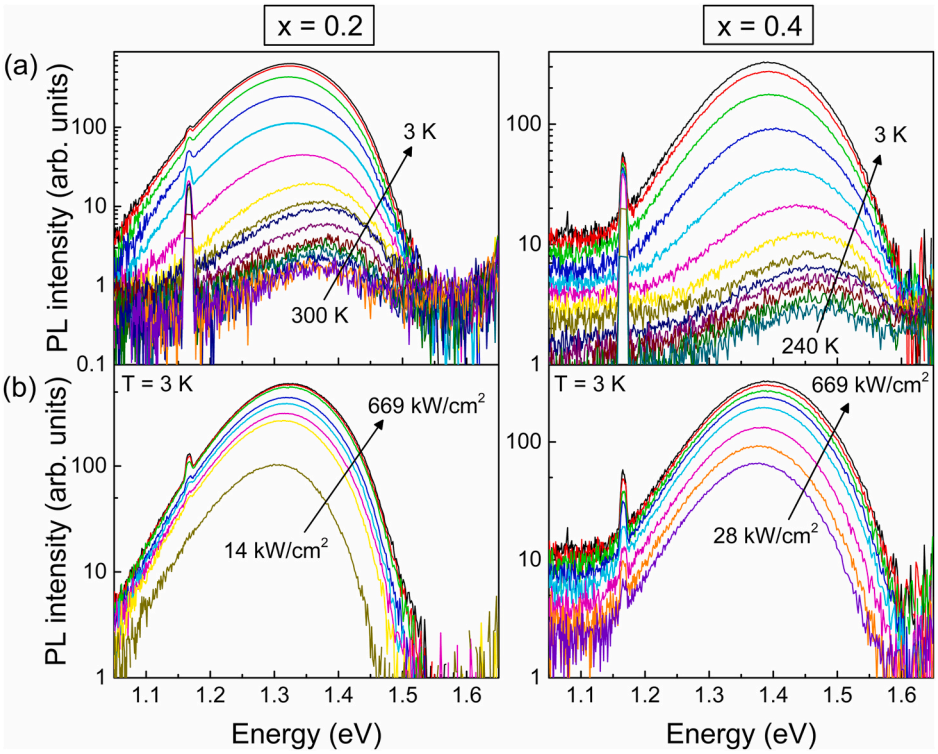

Fig. 7. (a) Temperature and **(b)** excitation power-dependent PL spectra of x = 0.2 and x = 0.4.

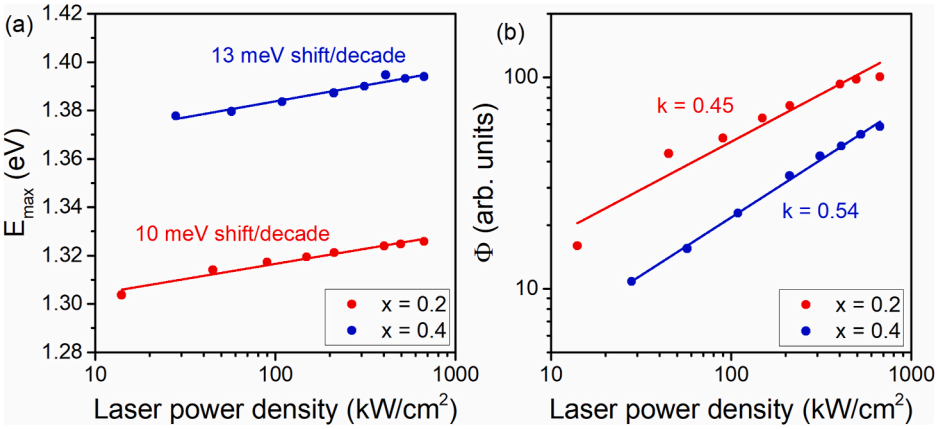

Fig. 8. Laser power dependence of the PL band: **(a)** E_{max} and **(b)** integrated intensity for x = 0.2 and x = 0.4. Experimental data was fitted by a linear equation.

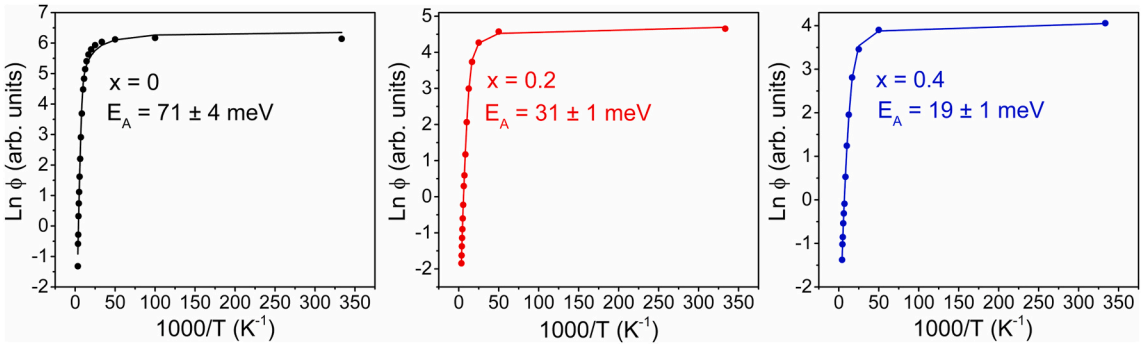

Fig. 9. Arrhenius plot derived from the temperature dependencies of the PL spectra for x = 0, x = 0.2 and x = 0.4. Activation energies (E_A) were calculated using the theoretical expression (1). Dots present the experimental data, while solid lines show the fitting result.

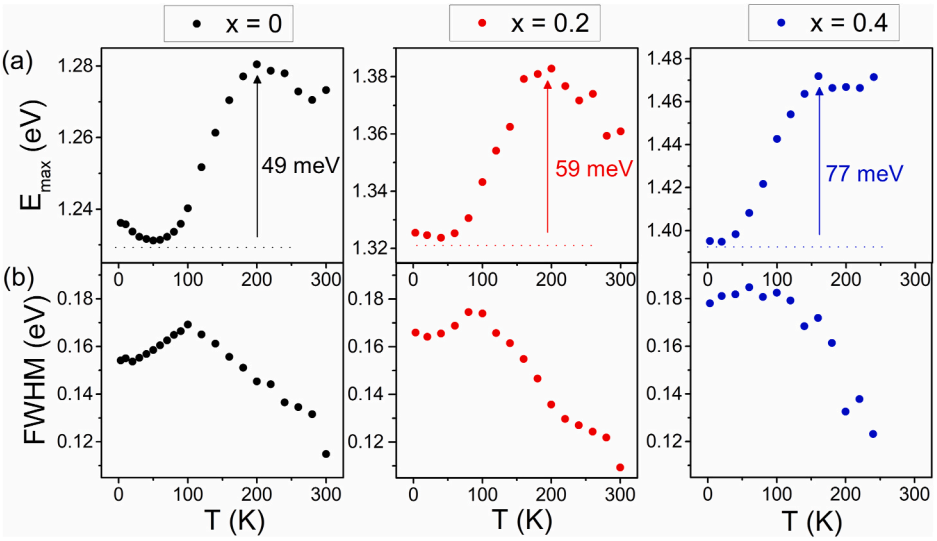

Fig. 10. Temperature dependence of the PL band **(a)** E_{max} and **(b)** FWHM for x = 0, x = 0.2 and x = 0.4.

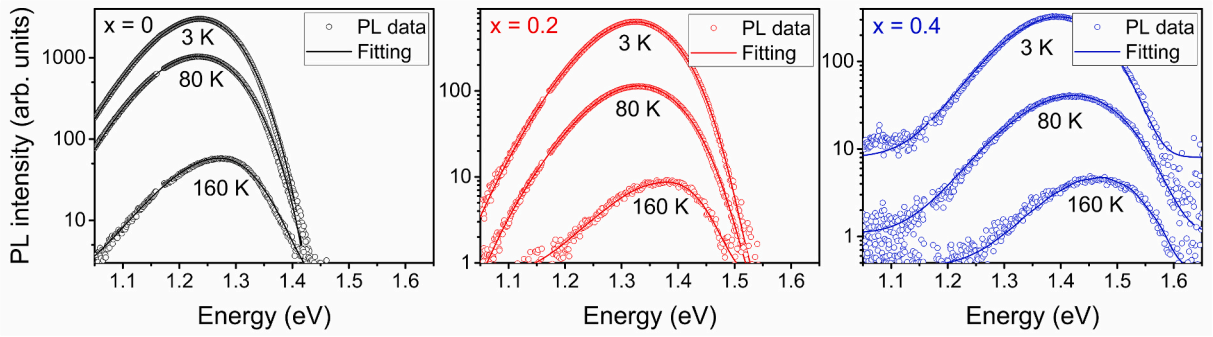

Fig. 11. The temperature evolution of the spectra for **(a)** x = 0, **(b)** x = 0.2 and **(c)** x = 0.4 fitted with the Pekarian function at 3 K, 80 K and 160 K. The data points which belong to the laser (266 nm) harmonics at around 1.16 eV were removed from the spectrum. Hollow circles show the measured PL data while continuous lines show the fitting spectra.

Table 3
PL parameters were obtained from the detailed analysis of the temperature dependence of the spectra. PL E_{max}, FWHM and γ (the average amplitude of fluctuations) values were obtained from the T = 3 K spectra. The max shift of E_{max} represents the difference between minimum and maximum values of E_{max}.

Sample	PL E_{max} (eV)	PL FWHM (meV)	E_A (meV)	γ (meV)	Max shift of E_{max} (meV)
x = 0	1.23	154	71	90	49
x = 0.2	1.32	165	31	95	59
x = 0.4	1.39	177	19	95	77

Depending on the shape of the emissions tail, Siebentritt et al. [70] have proposed different models. If the PL emission is defect-related, then the density of states function assumes a Gaussian shape. If the tails are treated like Urbach tails, then the density of states function assumes an exponential shape. Both types of shapes were previously detected in chalcopyrites and kesterites [61,71–73]. The average amplitude of fluctuations (γ) was calculated using the low-energy tail of emissions according to the Gaussian spectral dependence:

$$I(E) \sim exp\left(-\frac{(E-E_0)^2}{2\gamma^2}\right) \quad (3)$$

where $I(E)$ is the intensity of emission, E is photon energy and E_0 is the energy of the transition in unperturbed bands. The value of γ was determined to be around 90 meV, see Table 3.

There are two fundamental types of fluctuations within a semiconductor: electrostatic fluctuations (γ_{el}) and band gap fluctuations (γ_{bg}) [39]. The average amplitude of total fluctuations is given as:

$$\gamma = \sqrt{\gamma_{el}^2 + \gamma_{bg}^2} \quad (4)$$

Electrostatic fluctuations are formed by the charged defects inside the grains, at grain boundaries or interfaces. These charge states are caused by intrinsic structural defects and doping atoms [74]. On the other hand, the reasons for band gap fluctuations are attributed to spatial variations in composition, non-stoichiometry, tetragonal distortion in the lattice and ordering-disordering.

As given in Table 1, the standard deviation of elemental composition values for each sample increases slightly from x = 0 to x = 0.2 and then to x = 0.4. Again, the tetragonal distortion parameter declines linearly with an increase in Ge content with a slope of 1.567×10^{-2}, where the lattice diverges from the perfect tetragonal structure, $c/2a$ decreasing from 0.998 to 0.982 between CZTS and CZGS. These facts align with the slight increase of γ from samples with x = 0 to x = 0.4. The EDX analysis also shows that the ratio of Cu/(Zn + Sn + Ge) approaches stoichiometry with Ge incorporation. However, the ratios of Zn/(Sn + Ge) and metal/chalcogen do not exhibit a specific trend throughout the series, making it challenging to evaluate the effect of stoichiometry.

On the other hand, defect clusters in kesterite can cause local bandgap shifts up to 500 meV, which contributes γ_{bg} more significantly

than changes in stoichiometry [32]. Amongst them, $Cu_{Zn} + Zn_{Cu}$ defect cluster has the lowest formation energy, where the random distribution of Cu and Zn cations (Cu-Zn disorder) can induce a change in the bandgap energy up to 200 meV throughout the material [75]. In the CZTS lattice, the most energetically favorable condition is either fully disordered or ordered lattice. Assuming that the structure will always be partly disordered in all samples, we would expect the formation of separated disordered and ordered phases. These segregated phases with different bandgaps will significantly contribute to bandgap fluctuations [76].

3.7. Analysis and discussion of the radiative recombination mechanisms

The intensity of the PL spectra decreased with the increase of the Ge amount in the samples. PL I_{max} of x = 0.2 and x = 0.4 were determined to be 4 times and 8 times smaller compared to x = 0, respectively. This is an indication that defect-related non-radiative recombination starts prevailing in the system with Ge inclusion.

A high rate (more than several meV per decade) of blueshift with increased excitation power is typical for heavily doped semiconductors and is an indication of the presence of potential fluctuations in the material [37,40,77].

The temperature dependence can be analyzed in three regions. For the sample x = 0, at T = 3–40 K, E_{max} undergoes a small redshift of 5 meV, consistent with the bandgap shift in this temperature region [78]. At T = 50–200 K, E_{max} suffers a rather large blueshift of 49 meV and then shows a redshift again until RT. The rate of the redshift at T = 200–300 K cannot be accurately defined due to the increased noise in the spectra at high temperatures. Overall, the behavior of E_{max} after T = 50 K occurs due to the ionization of donor defects from wells below the conduction band. Since the activation energy of acceptors in all samples is a fraction of γ, it can be assumed that these are acceptor-like states in the valence band tails. The spatially varying bandgap will be a determinant for the depth of acceptor states in this case. Declining activation energies can also explain the increasing conductivity reported for the $Cu_2Zn(Sn_{1-x}Ge_x)S_4$ series [79]. All spectra exhibit a characteristic S-shaped behavior of $E_{max,}$ which has been observed previously when localized electron states were detected [68,80,81]. The dual redshift and blueshift behavior of E_{max} at low temperatures was earlier associated with donor defects distributed in deeper and shallower wells. The energy separation between these donor defects was indicated by the redshift of E_{max} in the very low-temperature region [81].

The significant difference between the bandgap and the PL peak position (>300 meV), as well as the small thermal activation energies (<80 meV), indicate that the most frequently observed BI, BT and BB recombination models of kesterite do not fit our measured spectra. Indeed, the temperature-dependent behavior of E_{max} is very similar to TI recombination. TI recombination can be seen in compensated semiconductors, where potential wells in the conduction band tail states can localize electrons. Due to localized electron states, the peak position typically shifts first to lower energies and then to higher energies as a result of the redistribution of carriers between shallower and deeper donor levels [33,68,82]. However, the critical temperature, where E_{max} transforms from redshift to blueshift is usually higher for TI, because more energy is needed for the liberation of carriers from tail states with different depths of energies. However, in our case, the initial redshift in low temperatures is much smaller, so it cannot be associated with this redistribution. Also, the donor defect levels in our case must be in a much deeper position that cannot overlap with the tail states.

To explain the low-temperature PL behavior of samples, two options are proposed: a deep donor-deep acceptor (DD-DA) recombination model or a defect cluster model. In a donor-acceptor pair (DAP) recombination, the binding energy between the donor and acceptor is modified by the Coulomb interaction so that the energy is distance-dependent [37,82]. The distance between the donor-acceptor pair is usually bigger than the lattice constant. When this distance becomes smaller, the recombination is referred to as DD-DA recombination [83,84]. Regarding the PL fitting results, our samples likely contain very closely located donor-acceptor defect pairs that have a deep position inside the bandgap. The typical behavior of DAP recombination in an ideal semiconductor with increasing laser power is a maximum blueshift of 2–3 meV per decade. This shift is due to the recombination probability for closer and distant pairs. On the other hand, the DD-DA pair model assumes more closely located defect pairs, which usually results in smaller blueshift or no blueshift at all. In our samples, the high rate of blueshift with increasing laser power suggests that the DD-DA model does not fit well. In fact, in the defect cluster model, a high blueshift with laser power is expected. Since the compensated defect clusters induce a significant bandgap decrease, also a discrepancy between PL E_{max} and E_g is expected [34]. These facts suggest that the defect cluster model is more suitable to describe our recombination model.

The width of the PL band is mainly affected by the interaction with optical phonons, electrons and fluctuations in the system. Typically, the PL band widens with increasing temperature [73]. The unusual decrease in FWHM after T = ~100 K suggests that in this region, there should be a contribution from at least two different recombinations in the system originating from very closely located PL emission bands. In order to understand the origin of these PL bands, the x = 0 spectra were fitted with two peaks, as shown in Fig. 12. Fitting was initiated using the PL E_{max} values at minima and maxima obtained from one-band fitting at T = 60–200 K. It is suggested that at T = 60–200 K, at least two PL bands coexist, where PL1 eventually quenches and PL2 prevails. At T = 200–300 K, the decrease in both E_{max} and FWHM (Fig. 10) could indicate that the coexisting recombinations in this temperature region have different origins or the related defects are ionizing at different temperatures. Also, the redshift in E_{max} at T = 200–300 K corresponds to the

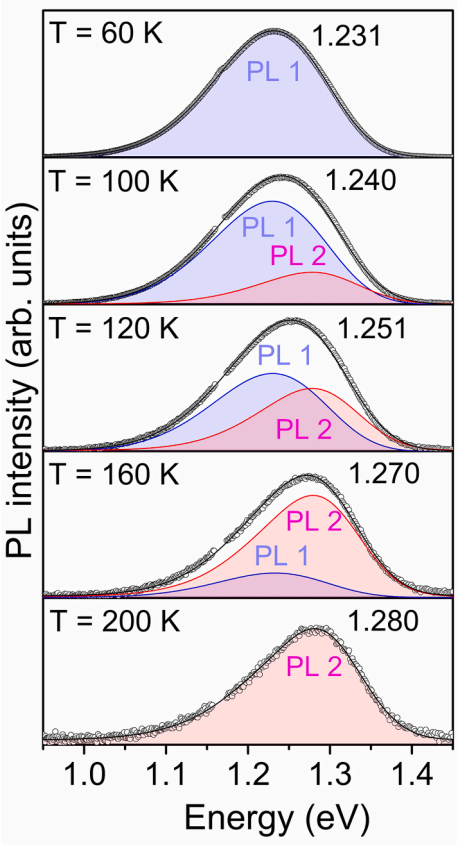

Fig. 12. Two-band recombination model showing the transformation of peaks at T = 60, 100, 120, 160 and 200 K. The peaks were fitted with the Pekarian function based on the x = 0 sample.

bandgap shift of CZTS in that temperature region. However, the mismatch between the PL E_{max} and E_g - E_A suggests that it cannot be easily attributed to a band-related recombination mechanism. After all, the reason behind the continuous decrease of FWHM after T = 200 K remains unclear.

Considering the defect cluster model [34], the focus should be on defect complexes rather than isolated defects. The most possible candidate for the donor defect is Sn_{Zn}, however, its ionization energy in the bandgap is deeper than what corresponds to our PL findings. Only when Sn_{Zn} forms a cluster with V_{Cu}, V_{Zn}, Zn_{Sn} or Cu_{Zn}, then the bandgap shift caused by these defect clusters correspond to our estimated acceptor (~50 meV from the valence band edge) and donor (~300 meV from the conduction band edge) ionization energies. Also, for the case of Zn_{Sn} + Sn_{Zn} and $2Cu_{Zn}$ + Sn_{Zn}, the formation energy of defect clusters decreases compared with the isolated Sn_{Zn} defect [32].

When Ge is incorporated into the system, some of the Sn_{Zn} is replaced by Ge_{Zn}, which has a deeper position in the bandgap, as predicted from PL E_{max} behavior. Additionally, according to theoretical calculations for CZTS and CZGS systems by Ratz et al., the formation energy of Ge_{Zn} is ~150 meV higher than Sn_{Zn} [26]. The reason behind this is that Ge has a more stable state at 4+ while Sn can easily switch between 4+ and 2+ oxidation states. This explains why the critical temperature in PL E_{max} behavior shifted to lower energies, as the carriers in donor wells started liberating at lower temperatures.

In summary, for all samples, a deep PL peak was observed, pointing to the defect cluster model. The dominating recombination should originate from defect clusters such as $2V_{Cu}$ + Sn_{Zn}, V_{Zn} + Sn_{Zn} Zn_{Sn} + Sn_{Zn} or $2Cu_{Zn}$ + Sn_{Zn}. In the mid-temperature region, the coexistence of two recombination mechanisms was observed. The behavior of E_{max} and FWHM with increasing temperature suggests that even in very high temperatures, deep donor defects remain and there is no transformation into band-related recombination. Ge incorporation didn't alter the dominating recombination mechanisms, instead, it changed their nature. Donor energy levels inside the bandgap shifted to deeper positions, while the carriers started ionizing earlier from donor wells. Further studies are needed to investigate the effects of these defect complexes in the $Cu_2Zn(Sn_{1-x}Ge_x)S_4$ system and find methods to suppress deep donor defects.

4. Conclusions

This study presented the compositional, structural and vibrational properties of wide-bandgap $Cu_2Zn(Sn_{1-x}Ge_x)S_4$ monograins, along with the device characteristics of MGL solar cells. Additionally, recombination mechanisms and related defects were investigated. Ge inclusion shifted the diffraction peaks to higher angles and decreased the unit cell volume. The tetragonal distortion parameters showed that all samples belong to the kesterite structure. In Raman spectra, a shift to higher wavenumbers of characteristic peaks was observed with the splitting of A_1 mode due to the coexistence of Ge-S and Sn-S bond between x = 0.2 and x = 0.8. As the bandgap increased, the V_{OC} slightly increased from 679 to 776 mV. The PL spectra of samples x = 0, x = 0.2 and x = 0.4 exhibited a wide, asymmetric-shaped peak at T = 3 K, shifting to higher energies with increased bandgap. As a result of temperature and laser power-dependent PL analysis, the dominant recombination was attributed to defect clusters involving a shallow acceptor and a deep donor defect. Findings from the temperature quenching of the PL revealed the presence of two-band spectra at T = 60–200 K. The candidates for dominating defect clusters have the deep donor defect Sn_{Zn} in common, which was partially suppressed by Ge substitution, as demonstrated by the shift of the critical temperature of PL E_{max}. As Ge content was increased, the acceptor ionization energy level decreased, while the donor defect level shifted into a deeper position. Overall, Ge alloying tuned the defect structure but did not affect the dominating recombination mechanism and the average amplitude of fluctuations. These results provide insight for further optimizing the composition and defect structure of Ge-alloyed CZTS toward achieving high-efficiency wide-bandgap solar cells.

CRediT authorship contribution statement

İdil Mengü: Writing – review & editing, Writing – original draft, Methodology, Investigation, Formal analysis, Data curation, Conceptualization. **Katri Muska:** Methodology. **Maris Pilvet:** Methodology. **Valdek Mikli:** Methodology. **Evelina Dudutienė:** Writing – review & editing, Investigation. **Rokas Kondrotas:** Methodology. **Jüri Krustok:** Writing – review & editing, Resources, Methodology, Formal analysis, Data curation, Conceptualization. **Marit Kauk-Kuusik:** Writing – review & editing, Supervision, Resources, Funding acquisition, Formal analysis, Conceptualization. **Maarja Grossberg-Kuusk:** Writing – review & editing, Supervision, Resources, Funding acquisition, Formal analysis, Conceptualization.

Declaration of competing interest

The authors declare that they have no known competing financial interests or personal relationships that could have appeared to influence the work reported in this paper.

Data availability

Data will be made available on request.

Acknowledgments

This work was supported by ERDF projects TK210, "NAMUR+ (2020.4.01.16–0123)", the Estonian Research Council grant PRG1023 and the European Union's H2020 research and innovation programme under Grant Agreement No. 952982.

References

[1] M. Grossberg, J. Krustok, C.J. Hages, D.M. Bishop, O. Gunawan, R. Scheer, S. M. Lyam, H. Hempel, S. Levcenco, T. Unold, The electrical and optical properties of kesterites, JPhys Energy 1 (2019) 044002, https://doi.org/10.1088/2515-7655/ab29a0.

[2] A. Wang, M. He, M.A. Green, K. Sun, X. Hao, A critical review on the progress of kesterite solar cells: current strategies and insights, Adv. Energy Mater. 13 (2023) 2203046, https://doi.org/10.1002/aenm.202203046.

[3] M.A. Green, E.D. Dunlop, M. Yoshita, N. Kopidakis, K. Bothe, G. Siefer, X. Hao, Solar cell efficiency tables (version 62), Prog. Photovoltaics Res. Appl. 31 (2023) 651–663, https://doi.org/10.1002/pip.3726.

[4] T. Unold, Accelerating research on novel photovoltaic materials, Faraday Discuss 239 (2022) 235–249, https://doi.org/10.1039/d2fd00085g.

[5] I. Kentaro, Copper Zinc Tin Sulfide-Based Thin-Film Solar Cells, John Wiley & Sons, UK, 2014.

[6] W. Shockley, H.J. Queisser, Detailed balance limit of efficiency of p-n junction solar cells, J. Appl. Phys. 32 (1961) 510–519, https://doi.org/10.1063/1.1736034.

[7] J. Kim, B. Shin, Strategies to reduce the open-circuit voltage deficit in $Cu_2ZnSn(S,Se)_4$ thin film solar cells, Electron, Mater. Lett. 13 (2017) 373–392, https://doi.org/10.1007/s13391-017-7118-1.

[8] T. Gershon, T. Gokmen, O. Gunawan, R. Haight, S. Guha, B. Shin, Understanding the relationship between $Cu_2ZnSn(S,Se)_4$ material properties and device performance, MRS Commun 4 (2014) 159–170, https://doi.org/10.1557/mrc.2014.34.

[9] J.J.S. Scragg, J.K. Larsen, M. Kumar, C. Persson, J. Sendler, S. Siebentritt, C. Platzer Björkman, Cu-Zn disorder and band gap fluctuations in $Cu_2ZnSn(S,Se)_4$: theoretical and experimental investigations, Phys. Status Solidi B 253 (2016) 247–254, https://doi.org/10.1002/pssb.201552530.

[10] M.Y. Valakh, A.P. Litvinchuk, V.M. Dzhagan, V.O. Yukhymchuk, Y.O. Havryliuk, M. Guc, I.v. Bodnar, V. Izquierdo-Roca, A. Pérez-Rodríguez, D.R.T. Zahn, Optical properties of quaternary kesterite-type $Cu_2Zn(Sn_{1-x}Ge_x)S_4$ crystalline alloys: Raman scattering, photoluminescence and first-principle calculations, RSC Adv. 6 (2016) 67756–67763, https://doi.org/10.1039/c6ra13608g.

[11] M. Ritzer, S. Schönherr, P. Schöppe, W. Wisniewski, S. Giraldo, G. Gurieva, A. Johannes, C.T. Plass, K. Ritter, G. Martínez-Criado, S. Schorr, E. Saucedo, C. Ronning, C.S. Schnohr, On the germanium incorporation in $Cu_2ZnSnSe_4$ kesterite solar cells boosting their efficiency, ACS Appl. Energy Mater. 3 (2020) 558–564, https://doi.org/10.1021/acsaem.9b01784.

[12] K. Biswas, S. Lany, A. Zunger, The electronic consequences of multivalent elements in inorganic solar absorbers: multivalency of Sn in Cu_2ZnSnS_4, Appl. Phys. Lett. 96 (2010) 201902, https://doi.org/10.1063/1.3427433.

[13] D.B. Khadka, J.H. Kim, Band gap engineering of alloyed $Cu_2ZnGe_xSn_{1-x}Q_4$ (Q = S, Se) films for solar cell, J. Phys. Chem. C 119 (2015) 1706–1713, https://doi.org/10.1021/jp510877g.

[14] S. Kim, K.M. Kim, H. Tampo, H. Shibata, S. Niki, Improvement of voltage deficit of Ge-incorporated kesterite solar cell with 12.3% conversion efficiency, App, Phys. Express 9 (2016) 102301, https://doi.org/10.7567/APEX.9.102301.

[15] Q. Guo, G.M. Ford, W.C. Yang, C.J. Hages, H.W. Hillhouse, R. Agrawal, Enhancing the performance of CZTSSe solar cells with Ge alloying, Sol. Energy Mater. Sol. Cells 105 (2012) 132–136, https://doi.org/10.1016/j.solmat.2012.05.039.

[16] D.B. Khadka, S.Y. Kim, J.H. Kim, Effects of Ge alloying on device characteristics of kesterite-based CZTSSe thin film solar cells, J. Phys. Chem. C 120 (2016) 4251–4258, https://doi.org/10.1021/acs.jpcc.5b11594.

[17] S. Oueslati, M. Grossberg, M. Kauk-Kuusik, V. Mikli, K. Ernits, D. Meissner, J. Krustok, Effect of germanium incorporation on the properties of kesterite $Cu_2ZnSn(S,Se)_4$ monograins, Thin Solid Films 669 (2019) 315–320, https://doi.org/10.1016/j.tsf.2018.11.020.

[18] A.D. Collord, H.W. Hillhouse, Germanium alloyed kesterite solar cells with low voltage deficits, Chem. Mater. 28 (2016) 2067–2073, https://doi.org/10.1021/acs.chemmater.5b04806.

[19] Y. Li, W. Ling, Q. Han, W. Shi, Colloidal $Cu_2Zn(Sn_{1-x}Ge_x)S_4$ nanocrystals: electrical properties and comparison between their wurtzite and kesterite structures, RSC Adv. 4 (2014) 55016–55022, https://doi.org/10.1039/c4ra10780b.

[20] I. Kim, K. Kim, Y. Oh, K. Woo, G. Cao, S. Jeong, J. Moon, Bandgap-graded $Cu_2Zn(Sn_{1-x}Ge_x)S_4$ thin-film solar cells derived from metal chalcogenide complex ligand capped nanocrystals, Chem. Mater. 26 (2014) 3957–3965, https://doi.org/10.1021/cm501568d.

[21] M. Umehara, S. Tajima, Y. Takeda, T. Motohiro, Wide bandgap $Cu_2ZnSn_{1-x}Ge_xS_4$fabricated on transparent conductive oxide-coated substrates for top-cells of multi-junction solar cells, J. Alloys Compd. 689 (2016) 713–717, https://doi.org/10.1016/j.jallcom.2016.08.039.

[22] E. Garcia-Llamas, J.M. Merino, R. Serna, X. Fontané, I.A. Victorov, A. Pérez-Rodríguez, M. León, I.V. Bodnar, V. Izquierdo-Roca, R. Caballero, Wide band-gap tuning $Cu_2ZnSn_{1-x}Ge_xS_4$ single crystals: optical and vibrational properties, Sol. Energy Mater. Sol. Cells 158 (2016) 147–153, https://doi.org/10.1016/j.solmat.2015.12.021.

[23] J.M. Cano-Torres, R. Caballero, I. Victorov, M. León, E. Garcia-Llamas, V. O. Yukhymchuk, A.M. Yaremko, Y.O. Havryliuk, I. Bodnar, J.M. Merino, Raman characterization and modelling of $Cu_2ZnSn_{1-x}Ge_xS_4$ single crystals grown using chemical vapor transport, Opt. Mater. 66 (2017) 671–677, https://doi.org/10.1016/j.optmat.2017.03.016.

[24] M.Y. Valakh, A.P. Litvinchuk, V.M. Dzhagan, V.O. Yukhymchuk, Y.O. Havryliuk, M. Guc, I.V. Bodnar, V. Izquierdo-Roca, A. Pérez-Rodríguez, D.R.T. Zahn, Optical properties of quaternary kesterite-type $Cu_2Zn(Sn_{1-x}Ge_x)S_4$ crystalline alloys: Raman scattering, photoluminescence and first-principle calculations, RSC Adv. 6 (2016) 67756–67763, https://doi.org/10.1039/c6ra13608g.

[25] G. Tseberlidis, V. Trifiletti, E. Vitiello, A.H. Husien, L. Frioni, M. Da Lisca, J. Alvarez, M. Acciarri, S.O. Binetti, Band-gap tuning induced by germanium introduction in solution-processed kesterite thin films, ACS Omega 7 (2022) 23445–23456, https://doi.org/10.1021/acsomega.2c01786.

[26] T. Ratz, N.D. Nguyen, G. Brammertz, B. Vermang, J.Y. Raty, Relevance of Ge incorporation to control the physical behaviour of point defects in kesterite, J. Mater. Chem. A 10 (2022) 4355–4365, https://doi.org/10.1039/d1ta09620f.

[27] A. Jimenez-Arguijo, A.G. Medaille, A. Navarro-Güell, M. Jimenez-Guerra, K. J. Tiwari, M. Placidi, M.S. Mkehlane, E. Iwuoha, A. Perez-Rodriguez, E. Saucedo, S. Giraldo, Z. Jehl Li-Kao, Setting the baseline for the modelling of Kesterite solar cells: the case study of tandem application, Sol. Energy Mater. Sol. Cells 251 (2023) 112109, https://doi.org/10.1016/j.solmat.2022.112109.

[28] M. Rudzikas, S. Pakalka, J. Donėlienė, A. Šetkus, Exploring the potential of pure germanium kesterite for a 2T kesterite/silicon tandem solar cell: a simulation study, Materials 16 (2023) 6107, https://doi.org/10.3390/ma16186107.

[29] B. Vermang, G. Brammertz, M. Meuris, T. Schnabel, E. Ahlswede, L. Choubrac, S. Harel, C. Cardinaud, L. Arzel, N. Barreau, J. Van Deelen, P.J. Bolt, P. Bras, Y. Ren, E. Jaremalm, S. Khelifi, S. Yang, J. Lauwaert, M. Batuk, J. Hadermann, X. Kozina, E. Handick, C. Hartmann, D. Gerlach, A. Matsuda, S. Ueda, T. Chikyow, R. Félix, Y. Zhang, R.G. Wilks, M. Bär, Wide band gap kesterite absorbers for thin film solar cells: potential and challenges for their deployment in tandem devices, Sustain. Energy Fuels 3 (2019) 2246–2259, https://doi.org/10.1039/c9se00266a.

[30] N. Saini, N.M. Martin, J.K. Larsen, A. Hultqvist, T. Törndahl, C. Platzer-Björkman, Record 1.1 V open-circuit voltage for Cu_2ZnGeS_4-based thin-film solar cells using atomic layer deposition $Zn_{1-x}Sn_xO_y$ buffer layers, Sol. RRL 6 (2022) 2100837, https://doi.org/10.1002/solr.202100837.

[31] Z. Guo, A.K. Jena, T. Miyasaka, Halide perovskites for indoor photovoltaics: the next possibility, ACS Energy Lett. 8 (2023) 90–95, https://doi.org/10.1021/acsenergylett.2c02268.

[32] S. Chen, A. Walsh, X.G. Gong, S.H. Wei, Classification of lattice defects in the kesterite Cu_2ZnSnS_4 and $Cu_2ZnSnSe_4$ earth-abundant solar cell absorbers, Adv. Mater. 25 (2013) 1522–1539, https://doi.org/10.1002/adma.201203146.

[33] J.P. Teixeira, R.A. Sousa, M.G. Sousa, A.F. Da Cunha, P.A. Fernandes, P.M. P. Salomé, J.P. Leitão, Radiative transitions in highly doped and compensated chalcopyrites and kesterites: the case of Cu_2ZnSnS_4, Phys. Rev. B 90 (2014) 235202, https://doi.org/10.1103/PhysRevB.90.235202.

[34] M. Grossberg, T. Raadik, J. Raudoja, J. Krustok, Photoluminescence study of defect clusters in Cu_2ZnSnS_4 polycrystals, Curr. Appl. Phys. 14 (2014) 447–450, https://doi.org/10.1016/j.cap.2013.12.029.

[35] K. Tanaka, T. Shinji, H. Uchiki, Photoluminescence from Cu_2ZnSnS_4 thin films with different compositions fabricated by a sputtering-sulfurization method, Sol. Energy Mater. Sol. Cells 126 (2014) 143–148, https://doi.org/10.1016/j.solmat.2014.03.052.

[36] T. Gershon, B. Shin, N. Bojarczuk, T. Gokmen, S. Lu, S. Guha, Photoluminescence characterization of a high-efficiency Cu_2ZnSnS_4 device, J. Appl. Phys. 114 (2013) 154905, https://doi.org/10.1063/1.4825317.

[37] X. Lin, A. Ennaoui, S. Levcenko, T. Dittrich, J. Kavalakkatt, S. Kretzschmar, T. Unold, M.C. Lux-Steiner, Defect study of $Cu_2ZnSn(S_xSe_{1-x})_4$ thin film absorbers using photoluminescence and modulated surface photovoltage spectroscopy, Appl. Phys. Lett. 106 (2015) 013903, https://doi.org/10.1063/1.4905311.

[38] E. Kask, M. Grossberg, R. Josepson, P. Salu, K. Timmo, J. Krustok, Defect studies in $Cu_2ZnSnSe_4$ and $Cu_2ZnSn(Se_{0.75}S_{0.25})_4$ by admittance and photoluminescence spectroscopy, Mater. Sci. Semicond. Process. 16 (2013) 992–996, https://doi.org/10.1016/j.mssp.2013.02.009.

[39] G. Rey, G. Larramona, S. Bourdais, C. Choné, B. Delatouche, A. Jacob, G. Dennler, S. Siebentritt, On the origin of band-tails in kesterite, Sol. Energy Mater. Sol. Cells 179 (2018) 142–151, https://doi.org/10.1016/j.solmat.2017.11.005.

[40] A.P. Levanyuk, V.V. Osipov, Edge luminescence of direct-gap semiconductors, Sov. Phys. Usp. 24 (1981) 187–215, https://doi.org/10.1070/PU1981v024n03ABEH004770.

[41] X. Zhu, J. Zhang, J. Liao, Q. Ru, W. Fu, Z. Wang, S. Xue, Transformation of carrier recombination mechanism as increasing the Germanium content in $Cu_2ZnGe_xSn_{1-x}S_4$ single crystal prepared by molten salt method, Opt. Mater. 139 (2023) 113744, https://doi.org/10.1016/j.optmat.2023.113744.

[42] K. Timmo, M. Pilvet, K. Muska, M. Altosaar, V. Mikli, R. Kaupmees, R. Josepson, J. Krustok, M. Grossberg-Kuusk, M. Kauk-Kuusik, Influence of alkali iodide fluxes on Cu_2ZnSnS_4 monograin powder properties and performance of solar cells, Mater. Adv. 4 (2023) 4509–4519, https://doi.org/10.1039/d3ma00444a.

[43] K. Muska, M. Kauk, M. Altosaar, M. Pilvet, M. Grossberg, O. Volobujeva, Synthesis of Cu_2ZnSnS_4 monograin powders with different compositions, Energy Proc. 10 (2011) 203–207, https://doi.org/10.1016/j.egypro.2011.10.178.

[44] K. Timmo, M.D. Sadurni, M. Pilvet, K. Muska, M. Altosaar, V. Mikli, F. Atlan, M. Guc, V. Izquierdo-Roca, M. Grossberg-Kuusk, M. Kauk-Kuusik, Efficiency enhancement of Cu_2ZnSnS_4 monograin layer solar cells via absorber post-growth treatments, Sol. Energy Mater. Sol. Cells 250 (2023) 112090, https://doi.org/10.1016/j.solmat.2022.112090.

[45] K. Timmo, M. Altosaar, J. Raudoja, M. Grossberg, M. Danilson, O. Volobujeva, E. Mellikov, Chemical etching of $Cu_2ZnSn(S,Se)_4$ monograin powder, IEEE Photovoltaic Specialists Conference (2010) 1982–1985, https://doi.org/10.1109/PVSC.2010.5616411.

[46] M. Kauk-Kuusik, K. Timmo, K. Muska, M. Pilvet, J. Krustok, R. Josepson, G. Brammertz, B. Vermang, M. Danilson, M. Grossberg, Detailed insight into the CZTS/CdS interface modification by air annealing in monograin layer solar cells, ACS Appl. Energy Mater. 4 (2021) 12374–12382, https://doi.org/10.1021/acsaem.1c02186.

[47] M. Kauk-Kuusik, K. Timmo, M. Pilvet, K. Muska, M. Danilson, J. Krustok, R. Josepson, V. Mikli, M. Grossberg-Kuusk, Cu_2ZnSnS_4 monograin layer solar cells for flexible photovoltaic applications, J. Mater. Chem. A 11 (2023) 23640–23652, https://doi.org/10.1039/d3ta04541b.

[48] D. Nam, S. Cho, J.H. Sim, K.J. Yang, D.H. Son, D.H. Kim, J.K. Kang, M.S. Kwon, C. W. Jeon, H. Cheong, Solar conversion efficiency and distribution of ZnS secondary phase in Cu_2ZnSnS_4 solar cells, Sol. Energy Mater. Sol. Cells 149 (2016) 226–231, https://doi.org/10.1016/j.solmat.2016.01.025.

[49] J. Chen, W. Li, C. Yan, S. Huang, X. Hao, Studies of compositional dependent $Cu_2Zn(Ge_xSn_{1-x})S_4$ thin films prepared by sulfurizing sputtered metallic precursors, J. Alloys Compd. 621 (2015) 154–161, https://doi.org/10.1016/j.jallcom.2014.09.097.

[50] A.R. Denton, N.W. Ashcroft, Vegard's law, Phys. Rev. A 43 (1991) 3161, https://doi.org/10.1103/PhysRevA.43.3161.

[51] Y. Zhang, X. Sun, P. Zhang, X. Yuan, F. Huang, W. Zhang, Structural properties and quasiparticle band structures of Cu-based quaternary semiconductors for photovoltaic applications, J. Appl. Phys. 111 (2012) 063709, https://doi.org/10.1063/1.3696964.

[52] M. Morihama, F. Gao, T. Maeda, T. Wada, Crystallographic and optical properties of $Cu_2Zn(Sn_{1-x}Ge_x)Se_4$ solid solution, Jpn. J. Appl. Phys. 53 (2014) 04ER09, https://doi.org/10.7567/JJAP.53.04ER09.

[53] G. Chen, W. Wang, S. Chen, Z. Whang, Z. Huang, B. Zhang, X. Kong, Bandgap engineering of $Cu_2ZnSn_{1-x}Ge_xS(e)_4$ by adjusting Sn-Ge ratios for almost full solar spectrum absorption, J. Alloys Compd. 718 (2017) 236–245, https://doi.org/10.1016/j.jallcom.2017.05.150.

[54] M. Grossberg, K. Timmo, T. Raadik, E. Kärber, V. Mikli, J. Krustok, Study of structural and optoelectronic properties of $Cu_2Zn(Sn_{1-x}Ge_x)Se_4$ (x = 0 to 1) alloy compounds, Thin Solid Films 582 (2015) 176–179, https://doi.org/10.1016/j.tsf.2014.10.055.

[55] E. Garcia-Llamas, J.M. Merino, R. Serna, X. Fontané, I.A. Victorov, A. Pérez-Rodríguez, M. León, I.v. Bodnar, V. Izquierdo-Roca, R. Caballero, Wide band-gap tuning $Cu_2ZnSn_{1-x}Ge_xS_4$ single crystals: optical and vibrational properties, Sol. Energy Mater. Sol. Cell. 158 (2016) 147–153, https://doi.org/10.1016/j.solmat.2015.12.021.

[56] J. He, L. Sun, S. Chen, Y. Chen, P. Yang, J. Chu, Composition dependence of structure and optical properties of $Cu_2ZnSn(S,Se)_4$ solid solutions: an experimental

study, J. Alloys Compd. 511 (2012) 129–132, https://doi.org/10.1016/j.jallcom.2011.08.099.
[57] M. Danilson, E. Kask, N. Pokharel, M. Grossberg, M. Kauk-Kuusik, T. Varema, J. Krustok, Temperature dependent current transport properties in Cu_2ZnSnS_4 solar cells, Thin Solid Films 582 (2015) 162–165, https://doi.org/10.1016/j.tsf.2014.10.069.
[58] M.A. Reshchikov, Mechanisms of thermal quenching of defect-related luminescence in semiconductors, Phys. Status Solidi (A) 218 (2021) 202000101, https://doi.org/10.1002/pssa.202000101.
[59] T. Schmidt, K. Lischka, W. Zulehner, Excitation-power dependence of the near-band-edge photoluminescence of semiconductors, Phys. Rev. B 45 (1991) 8989, https://doi.org/10.1103/PhysRevB.45.8989.
[60] K. Muska, K. Timmo, M. Pilvet, R. Kaupmees, T. Raadik, V. Mikli, M. Grossberg-Kuusk, J. Krustok, R. Josepson, S. Lange, M. Kauk-Kuusik, Impact of Li and K co-doping on the optoelectronic properties of CZTS monograin powder, Sol. Energy Mater. Sol. Cells 252 (2023) 112182, https://doi.org/10.1016/j.solmat.2023.112182.
[61] M. Grossberg, J. Krustok, J. Raudoja, K. Timmo, M. Altosaar, T. Raadik, Photoluminescence and Raman study of $Cu_2ZnSn(Se_xS_{1-x})_4$ monograins for photovoltaic applications, Thin Solid Films 519 (2011) 7403–7406, https://doi.org/10.1016/j.tsf.2010.12.099.
[62] J. Krustok, H. Collan, K. Hjelt, Does the low-temperature Arrhenius plot of the photoluminescence intensity in CdTe point towards an erroneous activation energy? J. Appl. Phys. 81 (1997) 1442–1445, https://doi.org/10.1063/1.363903.
[63] C. Spindler, F. Babbe, M.H. Wolter, F. Ehré, K. Santhosh, P. Hilgert, F. Werner, S. Siebentritt, Electronic defects in $Cu(In,Ga)Se_2$: towards a comprehensive model, Phys. Rev. Mater. 3 (2019) 090302, https://doi.org/10.1103/PhysRevMaterials.3.090302.
[64] S.I. Pekar, Theory of F-centers, J. Exptl. Theoret, Phys. (U.S.S.R.) 20 (1950) 510.
[65] K. Huang, A. Rhys, Theory of light absorption and non-radiative transitions in F-centres, Proc. Roy. Soc. Lond. A 204 (1950) 406–423, https://doi.org/10.1098/rspa.1950.0184.
[66] M. Nazarov, M.G. Brik, D. Spassky, B. Tsukerblat, A. Palii, A.N. Nazida, M. N. Ahmad-Fauzi, Phonon-assisted optical bands of nanosized powdery $SrAl_2O_4:Eu^{2+}$ crystals: evidence of a multimode Pekarian, Phys. Lett. 377 (2013) 3170–3178, https://doi.org/10.1016/j.physleta.2013.09.025.
[67] V.P. Dobrego, I.S. Shlimak, The influence of local potential fluctuations on the low-temperature radiative recombination of compensated gernianium, Phys. Status Solidi B 33 (1965) 805, https://doi.org/10.1002/pssb.19690330234.
[68] J. Krustok, T. Raadik, R. Kaupmees, M. Grossberg, M. Kauk-Kuusik, K. Timmo, A. Mere, Observation of band gap fluctuations and carrier localization in $Cu_2CdGeSe_4$, J. Phys. D Appl. Phys. 52 (2019) 285102, https://doi.org/10.1088/1361-6463/ab1afd.
[69] M.V. Yakushev, I. Forbes, A.V. Mudryi, M. Grossberg, J. Krustok, N.S. Beattie, M. Moynihan, A. Rockett, R.W. Martin, Optical spectroscopy studies of $Cu_2ZnSnSe_4$ thin films, Thin Solid Films 582 (2015) 154–157, https://doi.org/10.1016/j.tsf.2014.09.010.
[70] S. Siebentritt, N. Papathanasiou, M.C. Lux-Steiner, Potential fluctuations in compensated chalcopyrites, Phys. Rev. B Condens. Matter 376–377 (2006) 831–833, https://doi.org/10.1016/j.physb.2005.12.208.
[71] J.P. Leitão, N.M. Santos, P.A. Fernandes, P.M.P. Salomé, A.F. Da Cunha, J. C. González, G.M. Ribeiro, F.M. Matinaga, Photoluminescence and electrical study of fluctuating potentials in Cu_2ZnSnS_4-based thin films, Phys. Rev. B 84 (2011) 024120, https://doi.org/10.1103/PhysRevB.84.024120.
[72] A. Jagomägi, J. Krustok, J. Raudoja, M. Grossberg, M. Danilson, M. Yakushev, Photoluminescence studies of heavily doped $CuInTe_2$ crystals, Phys. Rev. B 337 (2003) 369–374, https://doi.org/10.1016/S0921-4526(03)00429-0.
[73] J. Krustok, R. Kaupmees, N. Abbasi, K. Muska, I. Mengü, K. Timmo, Bandgap fluctuations, hot carriers, and band-to-acceptor recombination in $Cu_2ZnSn(S,Se)_4$ microcrystals, Phys. Status Solidi 17 (2023) 2300077, https://doi.org/10.1002/pssr.202300077.
[74] J.H. Werner, J. Mattheis, U. Rau, Efficiency limitations of polycrystalline thin film solar cells: case of $Cu(In,Ga)Se_2$, Thin Solid Films (2005) 480–481, https://doi.org/10.1016/j.tsf.2004.11.052, 399–409.
[75] M. Valentini, C. Malerba, F. Menchini, D. Tedeschi, A. Polimeni, M. Capizzi, A. Mittiga, Effect of the order-disorder transition on the optical properties of Cu_2ZnSnS_4, Appl. Phys. Lett. 108 (2016) 211909, https://doi.org/10.1063/1.4952973.
[76] D.M. Bishop, B. McCandless, T. Gershon, M.A. Lloyd, R. Haight, R. Birkmire, Modification of defects and potential fluctuations in slow-cooled and quenched $Cu_2ZnSnSe_4$ single crystals, J. Appl. Phys. 121 (2017) 065704, https://doi.org/10.1063/1.4975483.
[77] B.I. Shklovskii, A.L. Efros, Electronic Properties of Doped Semiconductors, Springer Series in Solid-State Sciences, Berlin, 1984.
[78] P.K. Sarswat, M.L. Free, A study of energy band gap versus temperature for Cu_2ZnSnS_4 thin films, Phys. Rev. B Condens. Matter 407 (2012) 108–111, https://doi.org/10.1016/j.physb.2011.09.134.
[79] D. Mora-Herrera, M. Pal, F. Paraguay-Delgado, Facile solvothermal synthesis of $Cu_2ZnSn_{1-x}Ge_xS_4$ nanocrystals: effect of Ge content on optical and electrical properties, Mater. Chem. Phys. 257 (2021) 123764, https://doi.org/10.1016/j.matchemphys.2020.123764.
[80] H. Wang, Z. Ji, S. Qu, G. Wang, Y. Jiang, B. Liu, X. Xu, H. Mino, Influence of excitation power and temperature on photoluminescence in InGaN/GaN multiple quantum wells, Opt Express 20 (2012) 3932–3940, https://doi.org/10.1364/OE.20.003932.
[81] İ. Mengü, J. Krustok, R. Kaupmees, V. Mikli, M. Kauk-Kuusik, M. Grossberg-Kuusk, Radiative recombination pathways in ordered and disordered CZTSe microcrystals, Mater. Chem. Phys. 301 (2023) 127685, https://doi.org/10.1016/j.matchemphys.2023.127685.
[82] S. Oueslati, G. Brammertz, M. Buffière, C. Köble, T. Oualid, M. Meuris, J. Poortmans, Photoluminescence study and observation of unusual optical transitions in $Cu_2ZnSnSe_4$/CdS/ZnO solar cells, Sol. Energy Mater. Sol. Cells 134 (2015) 340–345, https://doi.org/10.1016/j.solmat.2014.10.041.
[83] J. Krustok, H. Collan, K. Hjelt, J. Mädasson, V. Valdna, Photoluminescence from deep acceptor-deep donor complexes in CdTe, J. Lumin. 72–74 (1997) 103–105, https://doi.org/10.1016/S0022-2313(97)00061-6.
[84] J. Krustok, T. Raadik, M. Grossberg, M. Kauk-Kuusik, V. Trifiletti, S. Binetti, Photoluminescence study of deep donor- deep acceptor pairs in Cu_2ZnSnS_4, Mater. Sci. Semicond. Process. 80 (2018) 52–55, https://doi.org/10.1016/j.mssp.2018.02.025.